Spektr: A computational tool for x-ray spectral analysis and imaging system optimization

J. H. Siewerdsen[a)]
Ontario Cancer Institute, Princess Margaret Hospital, Toronto, Ontario M5G 2M9, Canada
and Departments of Medical Biophysics and Radiation Oncology, University of Toronto, Toronto,
Ontario M5G 2M9, Canada

A. M. Waese
Department of Medical Biophysics, University of Toronto, Toronto, Ontario M5G 2M9, Canada

D. J. Moseley
Ontario Cancer Institute, Princess Margaret Hospital, Toronto, Ontario M5G 2M9, Canada

S. Richard
Department of Medical Biophysics, University of Toronto, Toronto, Ontario M5G 2M9, Canada

D. A. Jaffray
Ontario Cancer Institute, Princess Margaret Hospital, Toronto, Ontario M5G 2M9, Canada,
Departments of Medical Biophysics and Radiation Oncology, University of Toronto, Toronto,
Ontario M5G 2M9, Canada, and Radiation Medicine Program, Princess Margaret Hospital,
Toronto, Ontario M5G 2M9, Canada

A set of computational tools are presented that allow convenient calculation of x-ray spectra, selection of elemental and compound filters, and calculation of beam quality characteristics, such as half-value layer, mR/mAs, and fluence per unit exposure. The TASMIP model of Boone and Seibert is adapted to a library of high-level language (Matlab™) functions and shown to agree with experimental measurements across a wide range of kVp and beam filtration. Modeling of beam filtration is facilitated by a convenient, extensible database of mass and mass-energy attenuation coefficients compiled from the National Institute of Standards and Technology. The functions and database were integrated in a graphical user interface and made available online at http://www.aip.org/epaps/epaps.html. The functionality of the toolset and potential for investigation of imaging system optimization was illustrated in theoretical calculations of imaging performance across a broad range of kVp, filter material type, and filter thickness for direct and indirect-detection flat-panel imagers. The calculations reveal a number of nontrivial effects in the energy response of such detectors that may not have been guessed from simple K-edge filter techniques, and point to a variety of compelling hypotheses regarding choice of beam filtration that warrant future investigation. © *2004 American Association of Physicists in Medicine.* [DOI: 10.1118/1.1758350]

I. INTRODUCTION

Analysis of x-ray spectra and associated beam-quality characteristics [e.g., mR/mAs, half-value layer (HVL), and fluence per unit exposure (q_0/X)] is a topic of practical relevance in diagnostic medical physics and research of novel imaging systems. Diagnostic x-ray spectra have been thoroughly and accurately characterized by experimental measurements[1–3] and computational methods.[4] Recently, Boone and Seibert[5] reported on a method for computing x-ray spectra based on the method of interpolating polynomials. Called TASMIP, this model computes tungsten anode x-ray spectra in 1 keV energy bins between 30 and 140 kVp and provides accurate spectral estimation based on the measurements of Fewell *et al.*[2]

This article reports on two topics based on such spectral modeling. First, a straightforward adaptation of the TASMIP model to a flexible, extensible high-level language format (*viz.*, Matlab™, The MathWorks, Natick, MA) is described and made available for download (see Ref. 38). A library of functions for computing beam-quality characteristics was produced, along with a graphical user interface and a large database of mass and mass-energy attenuation coefficients compiled in a convenient format (*viz.*, Microsoft Excel). The library of Matlab™ functions, database of attenuation coefficients, and user interface is loosely termed Spektr.

Second, the flexibility and extensibility of the toolset are illustrated through analysis of imaging performance for a variety of active matrix flat-panel imager (FPI) systems across a broad range of kVp and added filtration. Spectral optimization is an important area of ongoing research in the application of FPIs in a variety of imaging applications. For example, in the early investigation of a-Se FPIs in mammography, Fahrig *et al.*[6] showed improved imaging performance for digital detectors at kVp higher than typical of screen-film

TABLE I. Summary of functions and data files included in the Spektr computational toolset.

MatLab Function	Description
Spectrum (kVp, mmA1, ripple)	Compute x-ray spectrum
Beers (q, [filters])	Filter the spectrum q by the materials and thicknesses in [filters]
Spektr	Launch Spektr graphical user interface
C2Compound (i)	Convert compound index i to chemical symbol
Compound2C (compound)	Convert chemical symbol to compound index
Element2Z (element)	Convert chemical symbol to atomic number
Equiv_mmAl ([filters])	Compute equivalent thickness in Al of materials and thicknesses in [filters]
Exposure (q)	Compute $\overline{mR/mAs}$ for the spectrum q at 100 cm from the focal spot
FluencePerExposure ( )	Compute $\overline{q_0/X}$ for the spectrum q at 100 cm from the focal spot
HVLn (q,n,Z)	Compute nth HVL for the spectrum q in the material Z
MeanEnergy (q)	Compute mean energy for the spectrum q
MuRhoCompound ([elements])	Compute $\mu/\rho(E)$ for the compound defined by the constituents in [elements]
Normalize (q)	Convert the spectrum q to a normalized probability distribution function
Z2Element (Z)	Convert atomic number Z to chemical symbol

Excel Workbook	Description
DensityCompounds.xls	Density of compounds available to the Spektr toolset
DensityElements.xls	Density of elements at STP for atomic numbers 1–92
MuRhoCompounds.xls	Linear and mass attenuation coefficients for available compounds
MuRhoElements.xls	Linear and mass attenuation coefficients for elements, $Z = 1-92$
TASMIP.xls	Fourth-order polynomial fit coefficients[5] for energies, $E = 0-150$ keV

mammography. For chest radiography, Dobbins *et al.*[7] demonstrated the improvement in contrast and signal-to-noise ratio to be gained through knowledgeable selection of kVp and filtration, indicating a clear trend toward heavier filtration (Cu) at high kVp. For cone-beam CT of the breast, Glick *et al.*[8] investigated optimal kVp using linear cascaded systems analysis,[9–11] finding optimal techniques in the range 40–50 kVp, depending on CsI:T1 converter thickness, anatomical background, and electronic noise. Similarly, McKinley *et al.*[12,13] have shown the strong potential for improved imaging performance in cone-beam CT of the breast using higher kVp and strong filtration. These investigations demonstrate improved imaging performance for FPIs through knowledgeable selection of kVp and filtration, with a trend toward higher kVp and heavier filtration emerging as a common theme.

While the main focus of this article is the computational toolset, its utility in spectral analysis and optimization was illustrated through calculation of imaging performance metrics [including detective quantum efficiency (DQE)] based on a theoretical linear cascaded systems model[9] for FPIs which has shown reasonable agreement with measurement.[14] The calculations are not intended as a rigorous investigation of the relative performance of various FPI systems. Rather, the analysis across a broad range of kVp, choice of filter materials, and thickness of added filtration is intended to illustrate the extensibility of the toolset, reveal nontrivial effects regarding choice of added filtration, and provide direction and hypotheses regarding spectral optimization for various FPI detector types, including direct and indirect-detection FPIs.

II. METHODS

A. X-ray spectral analysis using Spektr

Spektr was designed to provide a flexible, extensible tool for calculation of x-ray spectra, application of x-ray filters, and analysis of spectral characteristics—e.g., mR/mAs, HVL, and $\overline{q_0/X}$. The primary components of the tool are a library of Matlab™ functions [e.g., *spectrum*( ) and *beers*( ), below] and a database of x-ray attenuation coefficients for elements and compounds. The functions can be run from the Matlab™ command line or incorporated within scripts or other functions. The database includes mass and mass-energy attenuation coefficients for elements ($Z = 1-92$) and selected compounds gathered from the National Institute of Standards and Technology (NIST) tables.[15] The tool operates in the energy range 1–150 keV with 1 keV energy bins. A summary of the functions and database files comprising the Spektr toolset is shown in Table I.

1. The spectrum( ) function

The function *spectrum* (kVp, mm Al, ripple) is a straightforward adaptation of the TASMIP algorithm of Boone and Seibert[5] to Matlab™, with input arguments of tube potential (kVp), inherent or total Al filtration (mm Al), and % kV ripple. It operates over the same range of energies as TASMIP and at the same level of precision relative to the measured x-ray spectra of Fewell *et al.*[2]

2. The beers( ) function

The function *beers* (q, [filters]) filters a spectrum, q, [e.g., computed using *spectrum*( )] by the materials and thicknesses specified in [filters] according to Beer's law of expo-
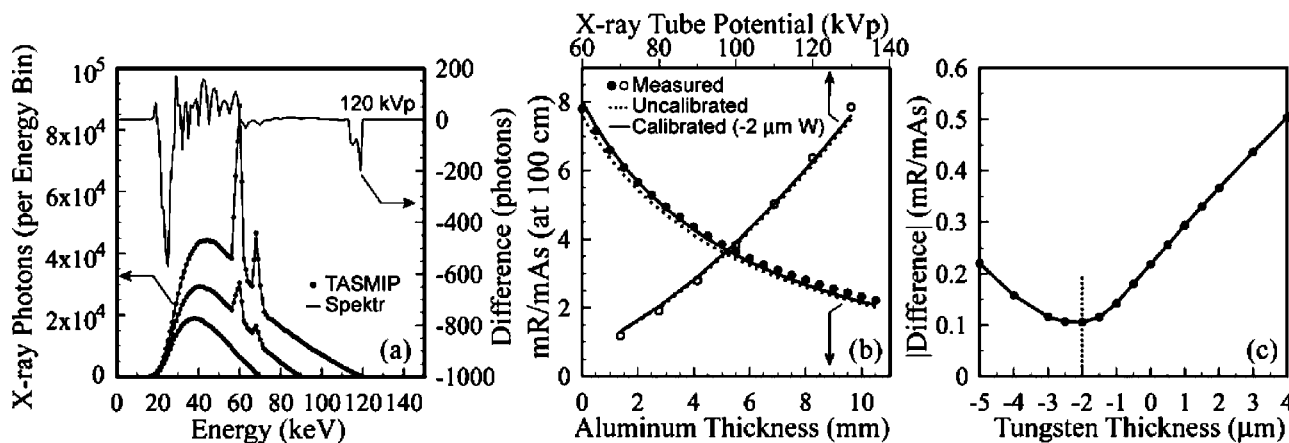
FIG. 1. Validation of Spektr calculations. (a) Comparison of TASMIP and Spektr calculations at 70, 90, and 120 kVp (left axis). Each case assumed 2.5 mm Al filtration and 5% kV ripple. The absolute difference between the spectra at 120 kVp is plotted on the right axis. (b) Tube output (mR/mAs) at 100 cm from the source as a function of added Al filtration (lower axis) and kVp (top axis). Measured values are plotted as solid and open circles, and Spektr calculations are shown as dashed and solid lines. (c) Difference between measured and calculated mR/mAs as a function of tungsten thickness. Calibration by -2 μm W filtration in Spektr calculations was found to minimize the discrepancy between measured and calculated values, improving agreement as shown in (b) for the solid ("calibrated") curve.

nential attenuation. The input parameter [filters] is an $N \times 2$ matrix, where each row corresponds to a given filter material—the first column specifying the material (for elements, $Z = 1 - 92$) and the second column specifying the thickness (mm). For example, *beers* (q, [13 10; 29 2]) computes the x-ray spectrum filtered by 10 mm Al and 2 mm Cu. A similar function, *beers_compound* (q, [filters]) filters the spectrum by compounds, with the first column of [filters] specifying the compound material. An extension (Sec. II A 4) allows filtration by arbitrary compounds with $\mu/\rho(E)$ computed by superposition.[16] Attenuation coefficients, $\mu/\rho(E)$ and $\mu_{ab}/\rho(E)$, were bicubic-interpolated to 1 keV bins, with interpolation below and above K edges handled separately to preserve K-edge structure.

The *beers*( ) function uses a database of mass attenuation coefficients gathered from NIST and compiled in a Microsoft Excel workbook. The workbook format was chosen for four main reasons: (1) the NIST data are irregularly binned and inconvenient to access directly from an automated tool; (2) this common, familiar format allows the user to view the data, plot, copy, and perform quick calculations in Excel; (3) extending the database to include additional materials is straightforward; and (4) the host application (Matlab™) provides built-in functionality for accessing workbooks via *xlsread*( ).

3. Validation

Spektr calculations were validated by comparing to TAS-MIP spectra[5] (which are known to agree within ~1% with the measurements of Fewell *et al.*)[2] and to measurements of photon output (mR/mAs). Example comparisons of Spektr and TASMIP spectra are in Fig. 1(a), showing only a slight discrepancy (~-0.6%) in the worst case, due primarily to slight differences in interpolated values of $\mu/\rho(E)$. Comparisons across a wide range of kVp, added filtration, and kV ripple exhibited similar or better agreement.

Spektr calculations were compared to measurements of photon output (mR/mAs) as a function of filter thickness and kVp. Measurements were performed on an x-ray imaging bench at 100 cm from the x-ray source (Rad94 x-ray tube in Varian sapphire housing) using an R100 diode and Barracuda exposure meter (RTI Electronics, Molndal, Sweden). The meter is specified by the manufacturer to provide accuracy better than 3% in exposure measurements from 50 to 150 kVp. Example comparisons are shown in Fig. 1(b) for mR/mAs as a function of added Al (bottom axis) and kVp (top axis). Although the calculations demonstrated reasonable agreement with measurements (~-3% to -5% discrepancy), we hypothesized that slight discrepancies could arise owing to anode angle, which is not accommodated in the TASMIP model. Therefore, calculations were repeated with varying thickness of tungsten filtration, and the mean difference from measurements was recorded, as shown in Fig. 1(c). A thickness of -1 to -2 μm W was found to minimize discrepancy (~-1% to -2%) and is consistent with hypothesis for the fairly large anode angle (14°) used in these measurements. This thickness was applied as a "calibration" included as inherent filtration for all subsequent calculations.

4. A graphical user interface

The Spektr functions and database were integrated in a simple graphical user interface (Spektr 1.0). The interface comprises six main groups of controls, labeled A–F in Fig. 2(a). Group A specifies the kVp, mm Al, and ripple input parameters to *spectrum*( ). A Tube Select drop-down menu allows the user to select from up to ten "tubes" for which calibrations (e.g., -2 μm W filtration) have been specified. Group B provides simple controls for the x-ray spectrum plot. Group C features a set of tools for calculating mR/mAs, HVL (first, second, and third HVL as well as tenth-value layer in Al or any element), normalization (conversion of x-ray spectrum to a probability distribution function), fluence
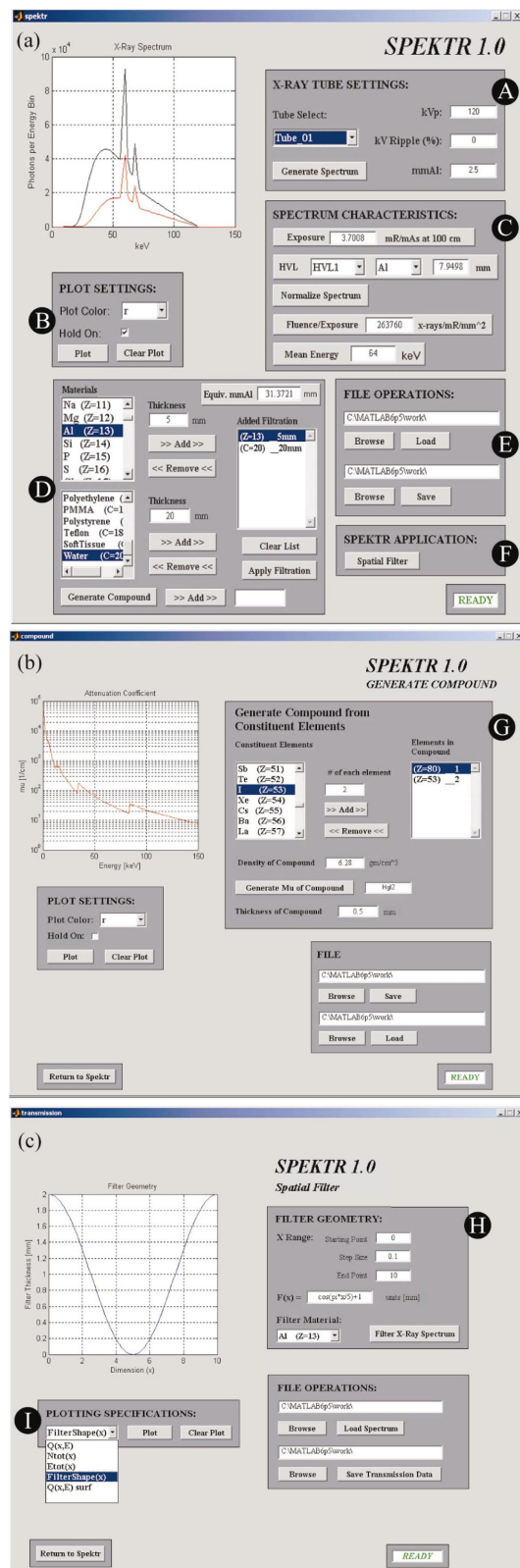
FIG. 2. A graphical user interface for x-ray spectrum analysis. (a) The main window features a set of tools (groups A–F) for generating and filtering x-ray spectra according to the *spectrum*( ) and *beers*( ) functions as well as computing a variety of spectral characteristics, including mR/mAs, HVL, fluence per unit exposure, and mean energy. (b) The Generate Compound tool launched from group D computes $\mu/\rho(E)$ for arbitrary compounds, passing the result back to the main window for addition in the Added Filtration. (c) The Spatial Filter tool launched from group F allows analysis of one-dimensional spatially varying filters.

per unit exposure ($\overline{q_0}/X$), and mean x-ray energy. Group D provides tools for changing applied filtration computed via *beers*( ). Elements and compounds are individually selected from the menus, thickness specified, and added to the list of added filtration. The menus include 92 elements ($Z = 1-92$) and 20 compounds corresponding to various biological[17] and detector[15] materials: adipose; air; blood; bone (cortical); brain; breast; CdTe; CsI; eye lens; Gd_2O_2S; GaAs; lung; HgI_2; muscle; polyethylene; polymethyl methacrylate; polystyrene; polytetrafluoroethylene (teflon); soft tissue; and water. The "Equiv. mm Al" tool computes the thickness of Al that would produce the same mR/mAs as the total filtration in the filter list.

The "Generate Compound" tool launched from group D [Fig. 2(b)] computes the mass attenuation coefficient, $\mu/\rho(E)$, for an arbitrary compound by superposition,[16] given the number and type of constituent elements and the density of the compound. The resulting $\mu/\rho(E)$ is passed back to the main application window to be appended to the list of added filters.

An additional tool, "Spatial Filter," [Fig. 2(c)] allows the user to specify one-dimensional spatially varying filters—useful, for example, in computing Heel effect or the effect of CT bow-tie filters, compensators, wedges, etc., on beam quality. The material and analytical shape of the filter are specified in group H. By selecting from the drop-down in group I, the user may plot the filter shape or visualize the spatially varying filtered spectrum in terms of total number of photons [denoted $N\text{tot}(x)$], total energy [denoted $E\text{tot}(x)$], or spectrum [a two-dimensional colorplot denoted $Q(x,E)$].

B. Application to imaging system optimization

1. Optimization of beam energy and added filtration for various detector types

The Spektr computational tools were used to investigate the performance of a variety of x-ray detectors under conditions of varying beam energy and added filtration. These calculations were intended primarily to illustrate the application and utility of the Spektr computational tools in an area of interest to the medical imaging community. They were not intended to provide definitive conclusion regarding optimal kVp and filtration nor compare the performance of various FPI designs. The results illustrate detector performance across a wide range of imaging conditions, revealing nontrivial trends in energy-dependent detector response and providing direction for future studies of system optimization.

As listed in Table II, four detector types were considered, corresponding to x-ray converter materials used in direct and indirect-detection active matrix FPIs.[18–21] Nominal detector design (e.g., converter thickness and pixel pitch) and imaging conditions (e.g., kVp and patient thickness) were chosen to correspond roughly to systems under development for a variety of applications. System #0 and #1 correspond to indirect-detection FPIs under development for cone-beam computed tomography (CBCT),[22] with nominal kVp, patient thickness, and exposure to the detector appropriate to CBCT of large anatomy. System #2 and #3 represent hypothetical

TABLE II. Summary of detector configurations and nominal imaging conditions. System #0 and #1 correspond to indirect-detection FPIs under development for cone-beam computed tomography. System #2 and #3 represent hypothetical direct-detection FPIs for radiography and fluoroscopy. For purposes of brevity, results are shown below for system #1 and #2 only, which represent two FPI detector types that are currently commercially available.

System #	Detector configuration			Imaging conditions			
	X-ray converter	Coverage (mg/cm^2)	Pixel pitch (mm)	kVp	mm Al	mm H$_2$O	X (mR)
#0	Gd$_2$O$_2$S:Tb	133	0.4	110	2.5	400	0.001
#1	CsI:Tl	250	0.4	110	2.5	400	0.001
#2	*a*-Se	214	0.2	70	2.5	200	0.01
#3	PbI$_2$	40	0.2	90	2.5	200	0.001

direct-detection FPIs, with nominal imaging conditions approximating radiographic and fluoroscopic imaging conditions, respectively.

Spectral characteristics and detector performance were computed as a function of kVp, filter material, and filter thickness for conditions based on the nominal settings in Table II. In each case, parameters such as fluence per unit exposure ($\overline{q_0}/X$), detector sensitivity (Γ, signal per pixel per unit exposure), and zero-frequency DQE (DQE$_0$), were computed as a function of kVp, filter material (Z_{filter} $= 1 - 92$), and filter thickness [characterized by material coverage, s_{filter} (mg/cm^2), equal to thickness times density]. Parameters describing detector performance were computed using simple cascaded systems analysis as described later. The results were examined for optimal choice of filter material and thickness—e.g., K-edge type filters that attenuate such that the x-ray spectrum incident on the detector is optimally matched to detector absorption efficiency, gain, etc.

2. Cascaded systems analysis

Spectral characteristics and detector performance parameters were computed according to well-known relations, and only a brief summary is provided here. The fluence per unit exposure, $\overline{q_0}/X$, was computed from the normalized x-ray spectrum, $q_{rel}(E)$, and definition of the Roentgen:[16]

$$\frac{\overline{q_0}}{X} = \int_0^\infty \frac{k\overline{q_{rel}}(E)}{E[\mu_{ab}(E)/\rho]_{air}} dE \quad (\text{x rays/mm}^2/\text{mR}), \quad (1)$$

where E is x-ray energy, $[\mu_{ab}/\rho]_{air}$ is the mass-energy absorption coefficient for air, k is a constant (5.45×10^8 eV/g/mR), and the integral over the energy domain is given by summation across the 1 keV bins used herein.

Detector performance was computed according to parameters estimated by cascaded systems analysis.[9] A number of simplifying assumptions were made herein, since the purpose of the calculations was primarily to illustrate the utility of the Spektr tools, rather than provide rigorous characterization of a given detector. Effects of depth-dependent absorption[23] and polyenergetic spectra[24] on image noise were neglected. A simple serial cascade was assumed, with effects of K-fluorescent x-rays[25–27] neglected. A unity fill factor was assumed throughout, and effects of noise-power aliasing[14,28,29] were neglected. Description of detector perfor-

mance by cascaded systems analysis has demonstrated reasonable agreement with experimental measurement,[14,30] and the simple model described here is condensed and simplified in order to highlight the dominant factors governing detector performance.

Given this simple linear model, the detector sensitivity, Γ, is given by:

$$\Gamma = \frac{\overline{q_0}}{X} a_{pix}^2 \overline{g_1}\, \overline{g_2}\, \overline{g_4} \quad (\text{electrons/pixel/mR}), \quad (2)$$

where a_{pix} is the pixel pitch (equal in this case to the pixel aperture), $\overline{g_1}$ is the quantum detection efficiency of the converting material, $\overline{g_2}$ is the mean gain (secondary quanta generated per interacting x ray—i.e., electrons/interaction or optical photons/interaction for direct or indirect-detection FPIs, respectively), and $\overline{g_4}$ is the coupling efficiency of secondary quanta to the pixel apertures. (Stage 3 represents the spatial spreading of secondary quanta, which is ignored in the zero-frequency analysis presented in this manuscript.) The zero-frequency DQE is given by:

$$DQE(0) = \frac{\overline{g_1}\, \overline{g_2}\, \overline{g_4}}{1 + (\overline{g_2} + \epsilon_{g2})\overline{g_4} + \dfrac{\sigma_{add}^2}{\Gamma X}}, \quad (3)$$

where ϵ_{g2} is the Poisson excess in secondary quanta and σ_{add} is the additive electronic noise (taken to be 1000 e for all detector systems in Table II).

The cascade parameters, $\overline{g_1}$, $\overline{g_2}$, ϵ_{g2}, and $\overline{g_4}$, were computed using incident x-ray spectra provided by Spektr. For example, $\overline{g_1}$ was computed from the mass attenuation coefficient of the detector material:

$$\overline{g_1} = \int_0^\infty \overline{q_{rel}}(E)\{1 - e^{-[\mu/\rho(E)]s}\} dE$$

$$(\text{interactions/incident x ray}), \quad (4a)$$

where μ/ρ and s refer to the detector. Similarly for the gain in secondary quanta:

$$\overline{g_2} = \frac{1}{\overline{g_1}} \int_0^\infty \overline{q_{rel}}(E)\{1 - e^{-[\mu/\rho(E)]s}\} \overline{g_2}(E) dE$$

$$(\text{secondary quanta/interaction}), \quad (4b)$$

where $\overline{g_2}(E)$ describes the energy-dependent gain in secondary quanta. For system #0 ($Gd_2O_2S:Tb$), values were taken from the measurements of Trauernicht *et al.*[31] For system #1–3, the gain was estimated analytically:

$$\overline{g_2}(E) = WE\,\eta_K(E)\,\eta_{esc} \quad \text{(secondary quanta/interaction)},$$

(4c)

where W is the number of secondary quanta generated per unit absorbed energy (quanta/keV), η_K is the energy absorption efficiency (i.e., the fraction of energy converted to secondary quanta, equal to 1 below the K edge and reduced by loss to K x rays above the K edge), and η_{esc} is the escape or collection efficiency of secondary quanta from the converting medium. For system #1, #2, and #3, W was approximated by values taken from the literature -50, 20, and 208 quanta/keV, respectively,[30,32] as was the fractional energy absorption efficiency. For system #1, the value of η_{esc} was taken conservatively to be a constant equal to 0.5 for the sake of simplicity, while for system #2 and #3 unity collection efficiency was assumed. The Poisson excess was estimated by averaging moments of the absorbed energy distribution over the absorbed spectrum, taken from measurements of Trauernicht[31] for system #0, from Swank for system #1,[33] and assumed near ideal (Swank factor=0.95) for system #2 and #3.[34,35] Finally, the coupling efficiency was taken to be 0.80 for system #0 (discrete "green" emission spectrum for $Gd_2O_2S:Tb$),[10] 0.65 for system #1 (broad "yellowish-white" emission spectrum for CsI:Tl),[36] and 1.0 for system #2 and #3.

III. RESULTS

The flexibility and extensibility provided by the Spektr functions and associated database are illustrated below in calculations of spectral characteristics and detector performance as a function of kVp, filter material, and filter thickness. The results are highly illustrative of complicated energy-dependent aspects of beam filtration and detector response and reveal a number of non-trivial effects.

A. Investigation of filter material type and thickness

The dependence of $\overline{q_0}/X$, Γ, and DQE_0 on filter material type ($Z_{filter} = 1-92$) and thickness (s_{filter}, mg/cm^2) was computed for the nominal conditions listed in Table II. Figure 3 shows $\overline{q_0}/X(Z_{filter},s_{filter})$ at energies of 70, 90, and 110 kVp (2.5 mm Al inherent filtration; 200 mm water). Common colorscales were used for ease of comparison. At lower kVp, there is a gradual increase in $\overline{q_0}/X$ with increasing atomic number out to $Z_{filter} \sim 55$. At higher kVp a more complex relationship in (Z_{filter}, s_{filter}) is revealed. Each case exhibits sudden reduction in $\overline{q_0}/X$ in the region $Z_{filter} \sim 55-69$ for all filter thicknesses, followed by an abrupt increase for $Z_{filter} > \sim 70$. The reduction occurs when the K edge of the filter (*viz.*, $E_K > \sim 35$ keV) is such that the transmitted spectrum suddenly exhibits a large proportion of low-energy x rays transmitted below E_K. The abrupt increase occurs when the K edge of the filter (*viz.*, $E_K > \sim 60$ keV) is such that the transmitted spectrum consists almost entirely of the lower-

energy component transmitted below the filter K edge. For $Z_{filter} > \sim 70$, the trend in $\overline{q_0}/X(Z_{filter}, s_{filter})$ is similar to that at low values of Z_{filter} for each kVp.

Of course, examination across this extremely broad range in Z_{filter} and s_{filter} implies very aggressive filtration (resulting in a nearly monoenergetic beam) for thick, high-Z filters. Correspondingly, the mR/mAs associated with such heavily filtered beams can be extremely low, as illustrated in Fig. 4, where mR/mAs is shown to diminish by one or more orders of magnitude, depending on filter material and thickness. Thus, the calculations herein are idealized in the sense that they assume the x-ray tube can provide sufficient output without regard for heat loading. While such idealization may push the current limits of x-ray tube technology, it is worthwhile to investigate what may be achieved in terms of detector performance if we allow ourselves to set tube loading considerations aside and shift an arbitrarily large burden to the x-ray tube.

Figure 5 shows the quantum detection efficiency, detector sensitivity, and zero-frequency DQE for two of the detector types in Table II. Calculations were performed for all four detector types, with results for the two most prevalent (CsI:Tl and *a*-Se) shown for purposes of brevity. For each detector, a resonance is observed over a fairly narrow range of Z_{filter} for which filtration of the beam matches the spectrum optimally to the detector attenuation coefficient. For example, we observe a peak in $\overline{g_1}$ in the region about $Z_{filter} \sim 73$ (Ta) for system #0 and #1, around $Z_{filter} \sim 58$ (Ce) for system #2, and around $Z_{filter} \sim 64$ (Gd) for system #3. Note that these optima do not quite correspond to what might be guessed from simple K-edge filtering, where a rule of thumb might suggest an optimal filter with atomic number (denoted Z_{filter}^*) between the K edges of a compound detector, or slightly higher than the effective atomic number of the detector (denoted Z_{det}^{eff}), or perhaps slightly higher than the heaviest constituent element in the detector (denoted Z_{det}'). Rather, the fairly complex spectra and attenuation coefficients in Eq. (4a) are such that optimal filters reside at values of Z related nontrivially to those of the detector. For example: system #0 ($Gd_2O_2S:Tb$; $Z_{det}^{eff}=60$; $Z_{det}'=64$; $Z_{filter}^* \sim 73$); system #1 (CsI:Tl; $Z_{det}^{eff}=54$; $Z_{det}'=55$; $Z_{filter}^* \sim 73$); system #2 (*a*-Se; $Z_{det}^{eff}=34$; $Z_{det}'=34$; $Z_{filter}^* \sim 58$); and system #3 (PbI_2; $Z_{det}^{eff}=69$; $Z_{det}'=82$; $Z_{filter}^* \sim 64$). The simple rule of thumb does not describe the optima for all cases (particularly the last case), and analysis of the spectra and attenuation coefficients—made trivial with the toolset described above—is essential to understanding the rather complicated effect. In each case, Z_{filter}^* introduces a fairly sharp cutoff in the filtered spectrum above the filter K edge, shaping the spectrum in a manner that is optimal in terms of detector DQE, including quantum detection efficiency ($\overline{g_1}$), sensitivity (Γ), etc.

Aside from the resonance near Z_{filter}^*, the behavior of $\overline{g_1}(Z_{filter}, s_{filter})$ exhibits a fairly monotonic decrease for thicker, higher-Z filters (due to higher mean energy of the beam). A plot of $\overline{g_2}(Z_{filter}, s_{filter})$ reveals a fairly monotonic trend for all detector types in which $\overline{g_2}$ increases for thicker,

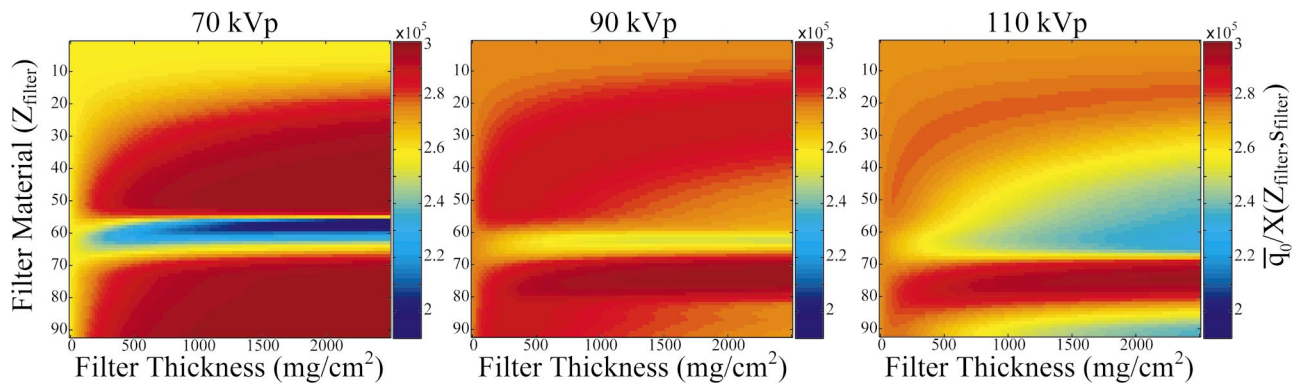FIG. 3. Fluence per unit exposure, $\overline{q_0}/X$ (photons/mm^2/mR), computed as a function of filter material type (Z_{filter}) and thickness (s_{filter},mg/cm^2) at 70, 90, and 110 kVp.

higher-Z filters. Therefore, $\Gamma(Z_{filter},s_{filter})$ as shown in Fig. 5 illustrates the tradeoff between $\overline{g_1}(Z_{filter},s_{filter})$ and $\overline{g_2}(Z_{filter},s_{filter})$. For system #0, #1, and #2 there is a gradual decrease in Γ for thicker, higher-Z filters [i.e., $g_1(Z_{filter},s_{filter})$ dominates]. For system #3 (not shown) we observe a peak in Γ extending in a band across filters ranging between $Z_{filter}\sim 20$–50. For all detectors, a distinct increase in Γ is observed in the region about Z^*_{filter} discussed above, where both $\overline{g_1}$ and $\overline{g_2}$ are high (and q_0/X is high as well).

Finally, calculations of $DQE_0(Z_{filter},s_{filter})$ are shown in Fig. 5. In each case, the zero-frequency DQE gradually degrades for thicker, higher-Z filters. However, the resonance in $\overline{g_1}$ and Γ is reflected in increased DQE in the region about
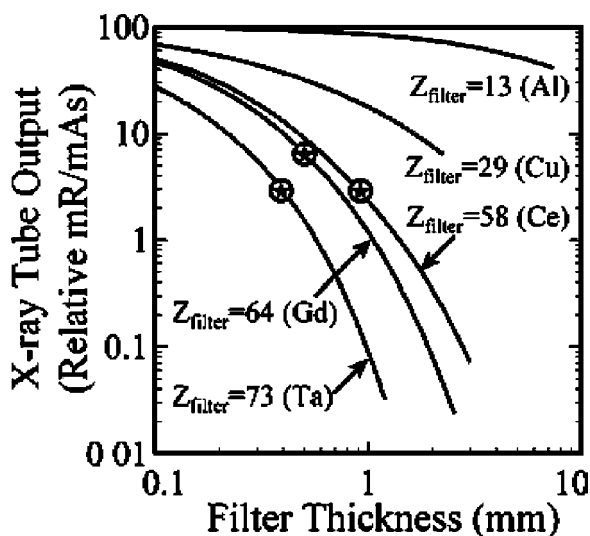

FIG. 4. Reduction in tube output for thick, high-Z filters. The vertical axis shows mR/mAs computed using Spektr for a nominal 120 kVp beam (2.5 mm Al inherent filtration), with values scaled to an arbitrary value of 100 for no added filtration. The horizontal axis is filter thickness (mm), and each curve covers a range in filter "coverage" or "thensity" (mg/cm^2) from 0 to 2000 mg/cm^2, which is the range of the horizontal axes in Figs. 3 and 5–7. These curves illustrate the effect of high-Z filter selection on tube output, showing reduction in mR/mAs by a factor of 10 to 1000, depending on filter type and thickness. Curves are shown for two common filters (Al and Cu) as well as three high-Z filters identified as possible optima for the various detector systems considered. The star symbols identify filter thicknesses as discussed in Sec. IV.

Z^*_{filter}. As described above, the filter material for which this optimum occurs is different from what might be hypothesized from a simple K-edge filter rule of thumb.

B. Investigation of kVp and beam filtration

Taking the optimal filter material suggested by the various Z^*_{filter} results of Fig. 5, the behavior of q_0/X, Γ, and DQE_0 were investigated as a function of kVp and filter thickness. In Fig. 6, q_0/X (kVp,s_{filter}) is shown for the three filter types: $Z^*_{filter}=58$, 64, and 73, respectively, revealing a complex dependence of fluence per unit exposure on kVp and filtration.

Figure 7 shows $\overline{g_1}$, Γ, and DQE_0 for two of the detector types in Table II, with choice of added filter given by Z^*_{filter} in each case. For each detector, a gradual decrease in g_1 is observed for higher kVp and thicker filtration, owing to higher mean energy of the beam. Γ(kVp,s_{filter}) again reveals the tradeoffs between $\overline{g_1}$(kVp,s_{filter}), $\overline{g_2}$(kVp,s_{filter}), and q_0/X(kVp,s_{filter}), and fairly complex, detector-specific relationships are revealed. Calculations of DQE_0(kVp,s_{filter}) suggest a fairly monotonic decrease with kVp for all detector types. For each detector at a given kVp, however, a significant increase in DQE is suggested by proper selection of filter thickness. For example: system #1 ($s_{filter}>\sim 800$ mg/cm^2 at 110 kVp); and system #2 ($s_{filter}>\sim 600$ mg/cm^2 at 70 kVp). These results suggest a lack of a strong optimum in kVp but are compelling in the potential for improved detector performance through knowledgeable selection of filter type (Z^*_{filter}) and thickness.

IV. DISCUSSION AND CONCLUSIONS

A convenient, extensible toolset for x-ray spectrum generation (based on the TASMIP model of Boone and Seibert),[5] filtration (using a database of attenuation coefficients compiled from NIST),[15] and calculation of spectral characteristics (including fluence-per-unit-exposure, HVLs, and mR/mAs) was reported and made available online (see Ref. 38). The toolset provides x-ray spectrum calculation from 1 to 150 keV in 1 keV energy bins using the TASMIP model of Boone and Seibert,[5] with polynomial coefficients contained in the data file *TASMIP.xls* in Table I. Extension to mammo-
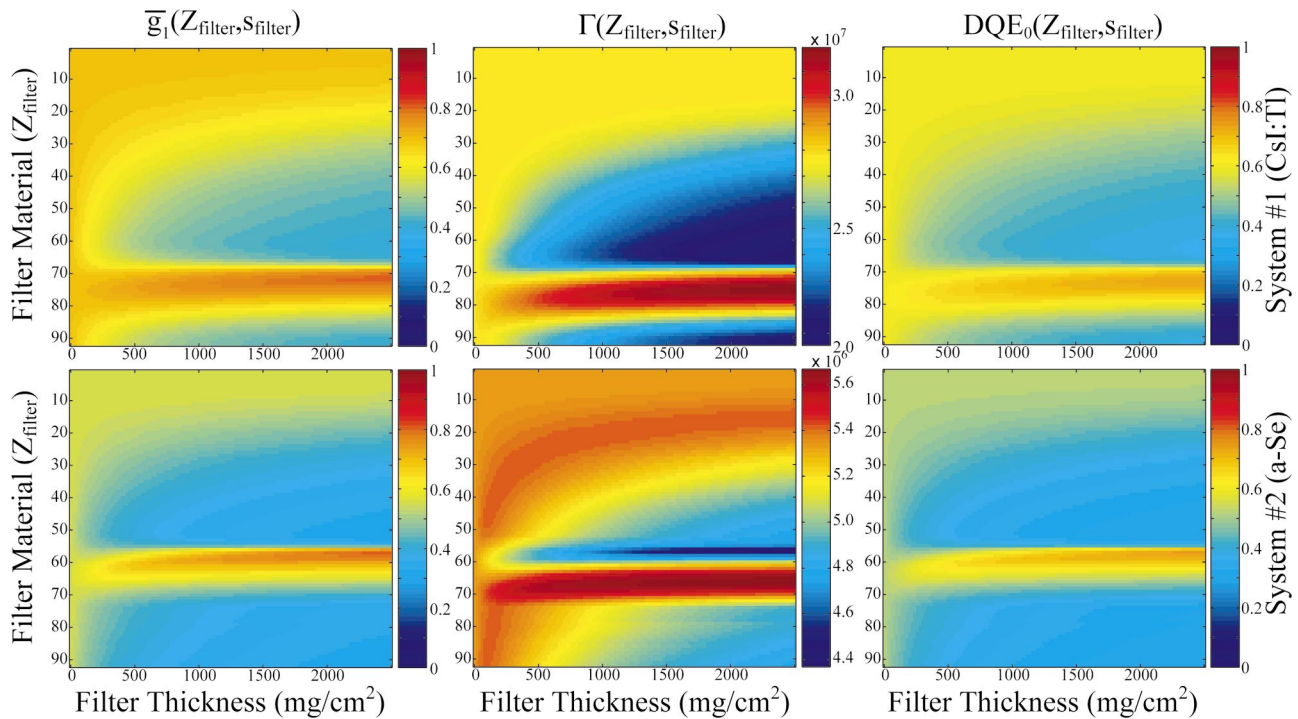
FIG. 5. Quantum detection efficiency ($\overline{g}_1$), detector sensitivity (Γ), and zero-frequency DQE computed as a function of filter material type (Z_{filter}) and thickness (s_{filter}) for two of the detector systems in Table I.

graphic spectra is fairly straightforward by replacement of the coefficients in *TASMIP.xls* with the MASMIP coefficients of Boone, Fewell, and Jennings,[37] although the toolset requires modification to 0.5 keV energy bins. The flexibility of the toolset was illustrated in calculation of detector performance across a broad range of kVp and beam filtration, highlighting a number of nontrivial trends in the energy-dependent response characteristics of direct and indirect-detection FPIs.

A simple linear cascaded systems model was applied to investigate the performance of various FPI designs across a broad range of x-ray spectra. This simple model has demonstrated reasonable agreement with measured results, but does not incorporate possible degradation in DQE due to depth-dependent absorption,[23] polyenergetic input spectrum,[24] or

K-fluorescence in the detector.[25–27] Since the objective of this study was to illustrate the Spektr toolset and investigate overall trends, rather than provide rigorous characterization or comparison of performance between FPIs, such effects were neglected. Furthermore, the results do not consider possible *K* fluorescence and reabsorption of fluorescent x rays within the beam filter itself. The calculations are exploratory and idealized in that they assume the x-ray tube can tolerate an arbitrarily large heat load burden, with sufficient output possible even for thick, high-*Z* filters. Furthermore, the calculations consider filtration of the spectrum in a manner that is optimized to detector response but do not consider the effect on subject contrast; extension of the calculations to consider specific imaging tasks is a subject of future work. Finally, investigations of DQE were limited to filters com-
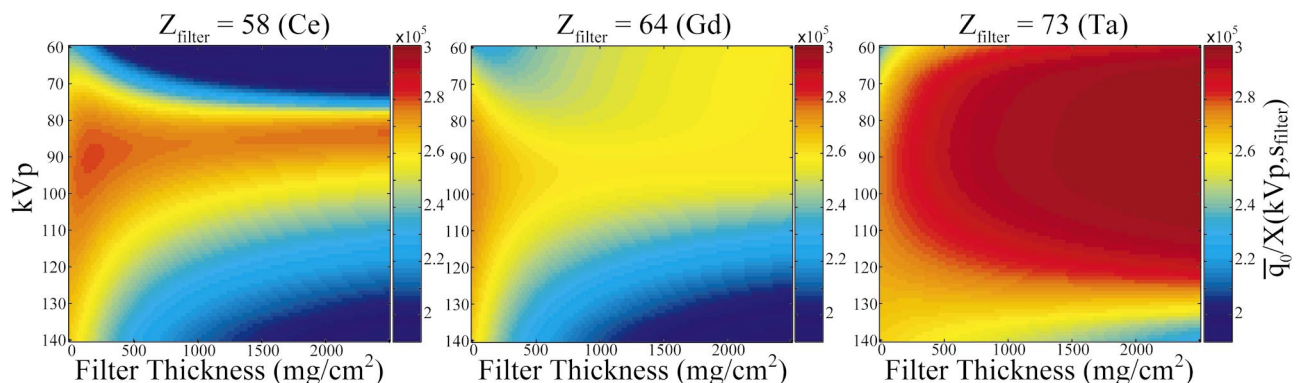

FIG. 6. Fluence per unit exposure, $\overline{q}_0/X$ (photons/mm^2/mR), computed as a function of kVp and filter thickness (s_{filter}) for three filter materials, $Z_{filter}^* = 58$, 64, and 73, for which increased DQE$_0$ was observed in Fig. 5.
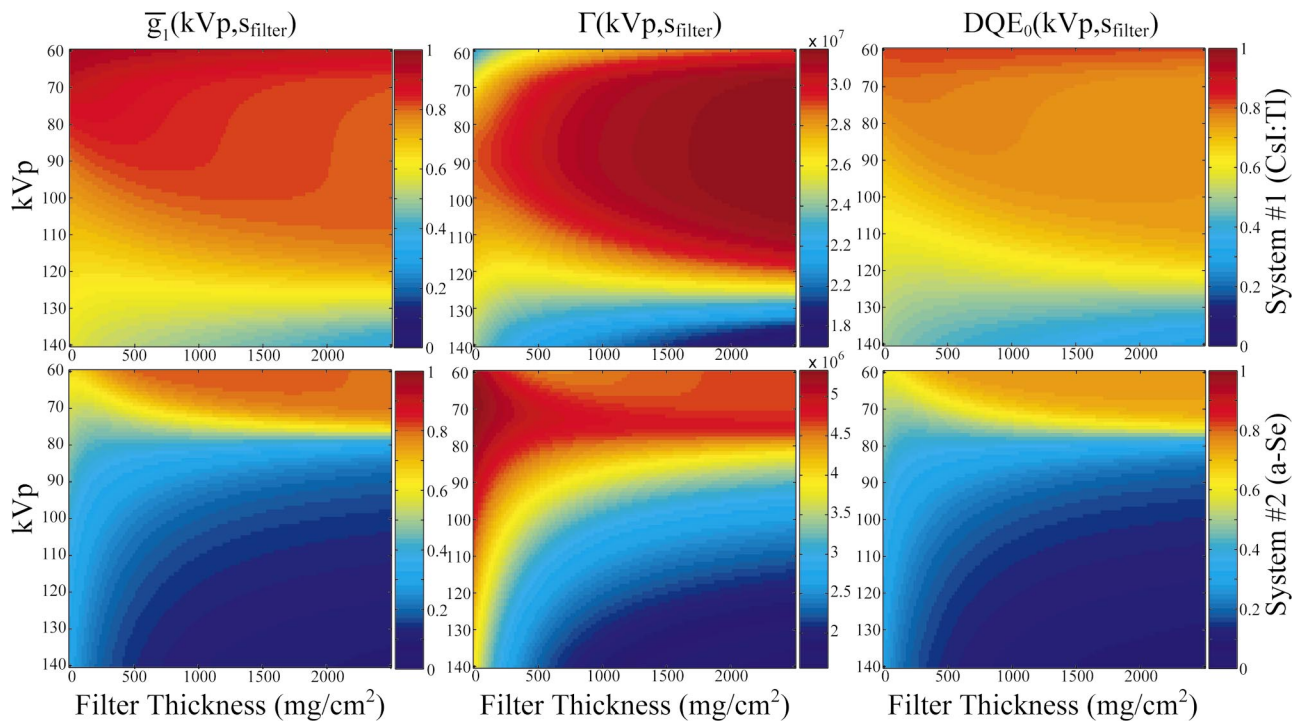
FIG. 7. Quantum detection efficiency ($\overline{g}_1$), detector sensitivity (Γ), and zero-frequency DQE computed as a function of kVp and filter thickness (s_{filter}) for two of the detector systems in Table I and added filtration of material type Z^*_{filter} [where $Z^*_{filter} = 73$ (Ta) for system #1, and $Z^*_{filter} = 58$ (Ce) for system #2].

posed of a single material type, although the Spektr toolset allows filtration by any number and composition of filters. Investigation of composite filters (e.g., Thoraeus filters,[16] in which a high-Z material is followed by a low-Z material) is a topic open to future investigation.

A number of interesting, nontrivial results were observed for various FPI designs. For system #0 and #1 (Gd_2O_2S:Tb and CsI:Tl-based FPIs, respectively), it was found that a fairly thin ($s_{filter} \sim 600$ mg/cm^2; ~ 0.4 mm) filter with $Z^*_{filter} = 73$ (Ta) could provide significant improvement in DQE. Similarly, system #2 (a-Se) suggested improvement for $Z^*_{filter} = 58$ (Ce; $s_{filter} \sim 600$ mg/cm^2; ~ 0.9 mm), as did system #3 (PbI$_2$) at $Z^*_{filter} = 64$ (Gd; $s_{filter} \sim 400$ mg/cm^2; ~ 0.5 mm). As illustrated in Fig. 4, in which the star symbol on the $Z_{filter} = 58$, 64, and 73 curves corresponds to these thicknesses, use of these filters shifts a large heat burden to the tube by diminishing tube output (mR/mAs) by more than a factor of 10. All systems exhibited a fairly monotonic decrease in DQE$_0$ with increasing kVp, suggesting the lack of a strong optimum in kVp, but with significant trends and possible optima in choice of filter type and thickness. The trends presented here were intended primarily to illustrate the utility of the Spektr toolset, and experimental validation is a subject open to future studies of spectral optimization.

The trends in system performance illustrated in this work would be difficult to ascertain without a flexible computational tool for x-ray spectral analysis, yet the toolset described makes such analysis straightforward and points to a variety of enticing research questions that are yet to be fully explored. While considerable attention has been paid to improving the design and performance of novel detectors such

as FPIs, comparably little has been paid to knowledgeable selection and control of the x-ray beam. Spectral optimization[6–8,12,13] is the first step in gaining such an understanding, with a variety of related investigations hopefully to follow.

For example, dynamic selection of beam kVp, filter material, and filter thickness for applications in which the exposure conditions change during an exam is a largely unexplored area of investigation and one that we hope is facilitated by a convenient computational toolset. Such applications include contrast-enhanced dual-subtraction imaging, dual-energy imaging, and multimode radiography/fluoroscopy. For the last case, we hypothesize that for a given detector configuration, the optimal kVp and filter would vary significantly between conditions where the detector is strongly quantum limited (e.g., a high-dose radiograph) and where the detector is electronic noise limited (e.g., low-dose fluoroscopy), and that dynamic filter selection could significantly improve image quality across all available imaging modes. In the field of multidetector CT, where there has been considerable progress in the design and performance of CT detectors, there is somewhat of a dearth in the literature regarding optimal selection of kVp and filtration for these new technologies. Similarly, spatially varying filters (e.g., "bowtie" filters) that quantitatively match the filter material and profile to the object size and FPI response characteristics is a topic yet to be fully explored, particularly in mammography and cone-beam CT. Finally, while it is recognized that the use of high-Z filters shifts a large heat burden to the x-ray tube, new imaging applications such as cone-beam CT are augmented in part by very efficient heat load

utilization (compared to fan-beam CT), creating an important opportunity to improve image quality through aggressive filter selection.

In summary, a convenient, extensible toolset for x-ray spectrum calculation, filtration, and computation of spectral characteristics was reported and made available online.[38] The tools demonstrate good agreement with measured HVL and mR/mAs, characteristics common to diagnostic imaging system evaluation and quality assurance. The tools provide convenient calculation of fluence per unit exposure, a parameter central to estimation of DQE. The toolset was exercised in a manner that illustrates its flexibility across a broad range of kVp, filter material, and filter thickness and highlights its potential in imaging system optimization. The illustrative calculations of detector performance as a function of kVp, Z_{filter}, and s_{filter} reveal nontrivial trends in system performance and point to a number of hypotheses regarding optimal kVp and filtration that warrant further investigation.

ACKNOWLEDGMENTS

[a] Author to whom correspondence should be addressed. Electronic mail: jsiewerd@uhnres.utoronto.ca

[1] T. R. Fewell and R. E. Shuping, "Photon energy distribution of some typical diagnostic x-ray beams," Med. Phys. **4**, 187–197 (1977).

[2] T. R. Fewell, R. E. Shuping, and K. R. Hawkins, *Handbook of Computed Tomography X-Ray Spectra* (U.S. Dept. of Health and Human Services, Public Health Service, Food and Drug Administration, Rockville, MD, 1981).

[3] R. Birch and M. Marshall, *Catalogue of Spectral Data for Diagnostic X-Rays* (The Hospital Physicists Association, London, 1979).

[4] D. M. Tucker, G. T. Barnes, and D. P. Chakraborty, "Semiempirical model for generating tungsten target x-ray spectra," Med. Phys. **18**, 211–218 (1991).

[5] J. M. Boone and J. A. Seibert, "An accurate method for computer-generating tungsten anode x-ray spectra from 30 to 140 kV," Med. Phys. **24**, 1661–1670 (1997).

[6] R. Fahrig, J. A. Rowlands, and M. J. Yaffe, "X-ray imaging with amorphous selenium: Optimal spectra for digital mammography," Med. Phys. **23**, 557–567 (1996).

[7] J. T. Dobbins III, E. Samei, H. G. Chotas, R. J. Warp, A. H. Baydush, C. E. Floyd, Jr., and C. E. Ravin, "Chest radiography: Optimization of x-ray spectrum for cesium iodide-amorphous silicon flat-panel detector," Radiology **226**, 221–230 (2003).

[8] S. J. Glick, S. Vedantham, and A. Karellas, "Investigation of optimal kVp setting for CT mammography using a flat-panel imager," Proc. SPIE **4682**, 392–402 (2002).

[9] I. A. Cunningham, M. S. Westmore, and A. Fenster, "A spatial-frequency dependent quantum accounting diagram and detective quantum efficiency model of signal and noise propagation in cascaded imaging systems," Med. Phys. **21**, 417–427 (1994).

[10] J. H. Siewerdsen, L. E. Antonuk, Y. El Mohri, J. Yorkston, W. Huang, J. M. Boudry, and I. A. Cunningham, "Empirical and theoretical investigation of the noise performance of indirect detection, active matrix flat-panel imagers (AMFPIs) for diagnostic radiology," Med. Phys. **24**, 71–89 (1997).

[11] I. A. Cunningham and R. Shaw, "Signal-to-noise optimization of medical imaging systems," J. Opt. Soc. Am. A **16**, 621–632 (1999).

[12] R. L. McKinley, M. P. Tornai, E. Samei, and M. L. Bradshaw, "Optimizing beam quality for x-ray computed mammotomography," Proc. SPIE **5030**, 575–584 (2003).

[13] R. L. McKinley, M. P. Tornai, E. Samei, and M. L. Bradshaw, "Simulation study of a quasimonochromatic beam for x-ray computed mammotomography," Med. Phys. **31**, 800–813 (2004).

[14] J. H. Siewerdsen, L. E. Antonuk, Y. El Mohri, J. Yorkston, W. Huang, and I. A. Cunningham, "Signal, noise power spectrum, and detective quantum efficiency of indirect-detection flat-panel imagers for diagnostic radiology," Med. Phys. **25**, 614–628 (1998).

[15] J. H. Hubbell and S. M. Seltzer, "Tables of x-ray mass attenuation coefficients and mass energy-absorption coefficients," http://physics.nist.gov/PhysRefData/XrayMassCoef/cover.html (2004).

[16] H. E. Johns and J. R. Cunningham, *The Physics of Radiology*, 4th ed. (Charles C. Thomas, Springfield, 1983).

[17] ICRU, "Tissue substitutes in radiation units and measurements," Report 44 (1988).

[18] W. Zhao, I. Blevis, S. Germann, J. A. Rowlands, D. Waechter, and Z. Huang, "Digital radiology using active matrix readout of amorphous selenium: Construction and evaluation of a prototype real-time detector," Med. Phys. **24**, 1834–1843 (1997).

[19] L. E. Antonuk, Y. el-Mohri, J. H. Siewerdsen, J. Yorkston, W. Huang, V. E. Scarpine, and R. A. Street, "Empirical investigation of the signal performance of a high-resolution, indirect detection, active matrix flat-panel imager (AMFPI) for fluoroscopic and radiographic operation," Med. Phys. **24**, 51–70 (1997).

[20] L. E. Antonuk, K. W. Jee, Y. El Mohri, M. Maolinbay, S. Nassif, X. Rong, Q. Zhao, J. H. Siewerdsen, R. A. Street, and K. S. Shah, "Strategies to improve the signal and noise performance of active matrix, flat-panel imagers for diagnostic x-ray applications," Med. Phys. **27**, 289–306 (2000).

[21] H. Hermon, M. Schieber, A. Zuck, A. Vilensky, L. Melekhov, E. Shiteki, A. Green, O. Dagan, S. E. Ready, R. A. Street, E. Seppi, R. Pavlyuchikova, G. Virshup, G. Zentai, and L. Partain, "Deposition of thick films of polycrystalline mercuric iodide x-ray detectors," Proc. SPIE **4320**, 133–139 (2001).

[22] D. A. Jaffray and J. H. Siewerdsen, "Cone-beam computed tomography with a flat-panel imager: Initial performance characterization," Med. Phys. **27**, 1311–1323 (2000).

[23] K. Rossmann and G. Lubberts, "Some characteristics of the line spread-function and modulation transfer function of medical radiographic films and screen-film systems," Radiology **86**, 235–241 (1966).

[24] M. J. Tapiovaara and R. F. Wagner, "SNR and DQE analysis of broad spectrum x-ray imaging," Phys. Med. Biol. **30**, 519–529 (1985).

[25] J. Yao and I. A. Cunningham, "Parallel cascades: New ways to describe noise transfer in medical imaging systems," Med. Phys. **28**, 2020–2038 (2001).

[26] W. Zhao, W. G. Ji, and J. A. Rowlands, "Effects of characteristic x rays on the noise power spectra and detective quantum efficiency of photoconductive x-ray detectors," Med. Phys. **28**, 2039–2049 (2001).

[27] A. Ganguly, S. Rudin, D. R. Bednarek, and K. R. Hoffmann, "Microangiography for neuro-vascular imaging. II. Cascade model analysis," Med. Phys. **30**, 3029–3039 (2003).

[28] I. A. Cunningham, "Degradation of the detective quantum efficiency due to a non-unity detector fill factor," Proc. SPIE **3032**, 22–31 (1997).

[29] J. P. Moy, "Signal-to-noise ratio and spatial resolution in x-ray electronic imagers: Is the MTF a relevant parameter?," Med. Phys. **27**, 86–93 (2000).

[30] W. Zhao and J. A. Rowlands, "Digital radiology using active matrix readout of amorphous selenium: Theoretical analysis of detective quantum efficiency," Med. Phys. **24**, 1819–1833 (1997).

[31] D. P. Trauernicht and R. Van Metter, "The measurement of conversion

noise in x-ray intensifying screens,'' Proc. SPIE **914**, 100–116 (1998).

[32] J. A. Rowlands and K. W. Taylor, ''Absorption and noise in cesium iodide x-ray image intensifiers,'' Med. Phys. **10**, 786–795 (1983).

[33] R. K. Swank, ''Absorption and noise in x-ray phosphors,'' J. Appl. Phys. **44**, 4199–4203 (1973).

[34] I. M. Blevis, D. C. Hunt, and J. A. Rowlands, ''X-ray imaging using amorphous selenium: Determination of Swank factor by pulse height spectroscopy,'' Med. Phys. **25**, 638–641 (1998).

[35] J. G. Mainprize, D. C. Hunt, and M. J. Yaffe, ''Direct conversion detectors: The effect of incomplete charge collection on detective quantum efficiency,'' Med. Phys. **29**, 976–990 (2002).

[36] U. W. Schiebel, N. Conrads, N. Jung, M. Weibrecht, H. Wieczorek, T. Zaengel, M. J. Powell, I. D. French, and C. Glasse, ''Fluoroscopic x-ray imaging with amorphous silicon thin-film arrays,'' Proc. SPIE **2163**, 129–140 (1994).

[37] J. M. Boone, T. R. Fewell, and R. J. Jennings, ''Molybdenum, rhodium, and tungsten anode spectral models using interpolating polynomials with application to mammography,'' Med. Phys. **24**, 1863–1874 (1997).

[38] See EPAPS Document No. E-MPHYA6-31-002407 to download the complete Spektr computational toolkit. A direct link to this document may be found in the online article's HTML reference section. The document may also be reached via the EPAPS homepage (http://www.aip.org/pubservs/epaps.html) or from ftp.aip.org in the directory /epaps/. See the EPAPS homepage for more information.